

Droplet absorption and spreading into thin layers of polymer hydrogels

Merlin A. Etzold¹, George T. Fortune¹, Julien R. Landel² and Stuart B. Dalziel¹

¹*Department of Applied Mathematics and Theoretical Physics,
Centre for Mathematical Sciences, University of Cambridge,
Wilberforce Road, Cambridge CB3 0WA, United Kingdom*

²*Department of Mathematics, Alan Turing Building,
University of Manchester, Oxford Road, Manchester, M13 9PL, UK*

(Dated: February 22, 2022)

From biological tissues to layers of paint, materials with the capacity to swell are ubiquitous. Here, we study experimentally and theoretically one of the conceptually simplest of such systems, the swelling of a thin hydrogel layer by a single water drop. Using a bespoke experimental setup, we observe fast absorption leading to a radially spreading axisymmetric blister. Employing a linear poroelastic framework and thin-layer scalings, we develop a non-linear one-dimensional diffusion equation for the evolution of the blister height profile, which agrees well with experimental observations.

High-swelling polymer systems, in particular hydrogels (hydrophilic polymers in water systems), have received considerable attention over recent years [1, 2]. Large volumetric strains, induced by slow swelling in response to changing environmental conditions, lead to a fascinating class of problems, where chemically-driven transport within the polymer drives large changes to the geometry of the hydrogel. These systems largely behave as hyper-elastic incompressible solids on short time scales [3].

Since the mechanical properties of hydrogels can be widely adjusted by changing the polymer chemistry and cross-linker density [4, 5], they have found wide-spread applications. The ability of external stimuli to trigger swelling that drives large deformations has been harnessed to drive microfluidic pumps [6, 7] and has led to their use as micro-actuators for optical, flow control, sensor and microrobotics applications [8, 9]. Understanding the interaction between swelling mechanics and microscopic driving forces is crucial for the design of these systems.

The excellent biocompatibility of hydrogels has ensured their use in biomedical applications [10] for over sixty years since the pioneering development of the soft contact lens [11]. Since their physico-chemical characteristics are similar to many tissues [12, 13], they have been used as tissue models in laboratory experiments (e.g. for decompression sickness; [14, 15]). In tissue engineering, they are used as a matrix framework for the repair and regeneration of a wide range of tissues and organs [16–18]. Hydrogel wound dressings have been developed that maintain a moist healing environment whilst allowing gaseous exchange, promoting wound healing [4, 19, 20].

These systems, characterised by complex interactions between biological materials and hydrogels, require a thorough understanding of hydrogel swelling behaviour. A good example of this interplay lies in the work of Cont *et al.* [21] who explore experimentally how *Vibrio cholerae* biofilms deform both thin hydrogel layers and epithelial cell mono-layers attached to the sur-

face of a soft extracellular matrix. The interactions between swelling and mechanical stresses cause the layers to buckle into the biofilm and, in many cases, break up. This shows a possible mechanism for a biofilm to compromise the physiology of its host and thus gain a competitive advantage when trying to survive in its chosen ecological niche.

A range of fully three-dimensional poroelastic theories for hydrogel swelling have been proposed. These theories derive a constitutive equation for the stress tensor from assumptions about the strain energy density function. While linear theories assume the function to be quadratic in the strain [3], non-linear theories [22–24] construct it from thermodynamic models for polymer deformation and polymer–solvent mixing [25]. These models become equivalent in the limit of small deformation [26]. Nevertheless, most experimental studies have considered one-dimensional or quasi-one dimensional geometries only, e.g. the swelling of fibres [27], spheres [28–30] or flat sheets bound to surfaces [28]. In other cases, finite element methods are used to solve more complicated problems such as the swelling caused by droplet trains [31]. However, considerable challenges remain, especially for high-swelling systems producing large swelling gradients. [32].

Inspired by the flat geometries found in cell layers [21], wound dressing [4] and hydrogel water harvesters [33], in this letter we investigate experimentally and theoretically the absorption and spreading of a single droplet of water into a thin hydrogel layer. This is also a model system for the absorption of more hazardous substances into thin layers of paints and coatings [34]. This is analogous to the injection of a finite volume of fluid into thin poroelastic layers, a well-studied canonical fluid dynamics problem (e.g. [35]), which leads to blister formation and its slow outward spreading.

We used commercially available hydrogel pads that were glued onto standard microscope slides and then placed in a mineral-oil filled bath (see figure 1). The hy-

drogel was then observed through windows in the bath against near-collimated background illumination. The purpose of the mineral oil was to suppress vapour phase transport. Full experimental details are given in Supplementary Material [36] and representative profile data is provided as Electronic Supplementary Information (ESI).

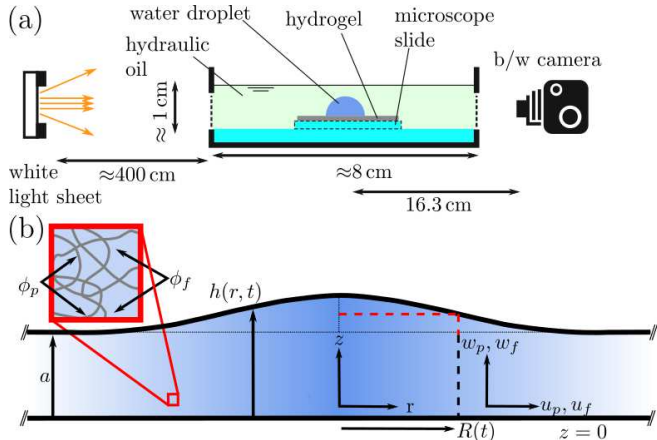


FIG. 1. (a) Experimental apparatus. (b) Hydrogel sheet schematic. An axisymmetric blister (blue) with characteristic radius $R(t)$ spreads between a rigid surface at $z = 0$ and a free surface at $z = h$, with undeformed height a . The pore-averaged velocities of the solid and fluid phases are denoted by $\mathbf{u}_p = (u_p, w_p)$ and $\mathbf{u}_f = (u_f, w_f)$. For comparison with experimental and numerical data we take $R(t)$ as the point at which the blister height decreases to half of its maximum value (red dashes line). Inset: the hydrogel is a mixture of polymer (grey, volume fraction ϕ_p) and water (blue, volume fraction $\phi_f = 1 - \phi_p$)

Typical experimental footage for a 100 μl droplet is shown in figure 2. Due to refraction, the droplet and hydrogel appear dark. The upper edge of the hydrogel was located using automatic image analysis [37, 38]. The hydrogel swelling had three distinct phases. In the first phase, which lasted about 10 min once the water had reached a sessile drop state on the hydrogel surface (after approximately 30 s), surface water and swollen hydrogel coexisted as the sessile droplet transformed into a swollen blister (figures 2(a-c)). This transition was particularly apparent at the droplet edge, which became progressively steeper (figure 2(c)) before becoming smooth again. In the second phase, once all the surface water had been absorbed, a surface instability appeared, forming a blister with a crinkled surface (figures 2(e-g)). This buckling instability is known in the literature, arising in hydrogels that have strong swelling gradients or are laterally confined [39, 40]. Supplementary experiments in air, where the water was removed at various stages in the first phase, found a thin swollen layer with the same surface instability whose wavelength increased with time. Hence, we conclude that this instability forms immediately after the

droplet reaches the gel, but only becomes visible once the droplet has been absorbed. In the third phase, until experiments were terminated once the blister front had reached the edge of the hydrogel, the buckling instability vanished as the blister assumed a self-similar shape resembling a non-linear diffusion process as the blister appears to evolve in a nonlinear fashion with a self-similar profile (figures 2(h-l)). Further experimental aspects are reported in [36].

Motivated by the self-similar profile observed in phase three of the experiments, we now develop a mathematical model for the swelling hydrogel layer using a poroelastic framework to obtain a non-linear diffusion equation describing its spreading dynamics. We consider a system in which the dynamics are governed by the interplay between the motion of both polymer and water and the balance of elastic stresses through the polymer network. Figure 1(b) sketches the surface of a hydrogel layer of undeformed thickness a , fixed to a rigid horizontal boundary at $z = 0$. The gel is perturbed through the addition of a spherical water drop of diameter d , forming an axisymmetric blister of height profile $h(r, t)$ and radius $R(t)$. We examine the simplest hydrogel composition, namely a solution of polymer (volume fraction ϕ_p , where $\phi_p = \phi_{0p}$ at the start of the experiment before the water drop is added) and water (modelled as a Newtonian fluid with volume fraction $1 - \phi_p$). We denote the pore-averaged velocity and Cauchy stress tensor of the solid and liquid phases by $\{\mathbf{u}_p = (u_p, w_p), \boldsymbol{\sigma}_p\}$ and $\{\mathbf{u}_f = (u_f, w_f), \boldsymbol{\sigma}_f \approx -p\mathbf{I}\}$ respectively, where p is the pore pressure and \mathbf{I} the identity tensor. Conservation of mass in the solid and fluid phases gives

$$\frac{\partial \phi_p}{\partial t} + \nabla \cdot (\phi_p \mathbf{u}_p) = 0, \quad -\frac{\partial \phi_p}{\partial t} + \nabla \cdot ((1 - \phi_p) \mathbf{u}_f) = 0. \quad (1)$$

Similarly, a momentum balance yields

$$\nabla \cdot \boldsymbol{\sigma} = \nabla p, \quad (2)$$

where $\boldsymbol{\sigma}$ obeys the elastic constitutive law,

$$\boldsymbol{\sigma} = \boldsymbol{\sigma}(\nabla \boldsymbol{\xi}), \quad (3)$$

and $\boldsymbol{\xi} = (\xi, \zeta)$, the deformation of the medium away from a reference state. This deformation is related to the velocity of the polymer phase through $\mathbf{u}_p = (\partial_t + \mathbf{u}_p \cdot \nabla) \boldsymbol{\xi}$. Here, we consider the simplest case, where $\boldsymbol{\sigma}$ obeys the linear constitutive law

$$\boldsymbol{\sigma} = \left(K - \frac{2G}{3} \right) (\nabla \cdot \boldsymbol{\xi}) \mathbf{I} + G(\nabla \boldsymbol{\xi} + \nabla \boldsymbol{\xi}^T), \quad (4)$$

with K and G are the osmotic and shear moduli of the hydrogel respectively, assumed constant [22, 41]. We close the system of equations (1)–(2) by invoking Darcy's law for fluid motion within the matrix,

$$(1 - \phi_p)(\mathbf{u}_p - \mathbf{u}_f) = \frac{\kappa}{\mu_f} \nabla p. \quad (5)$$

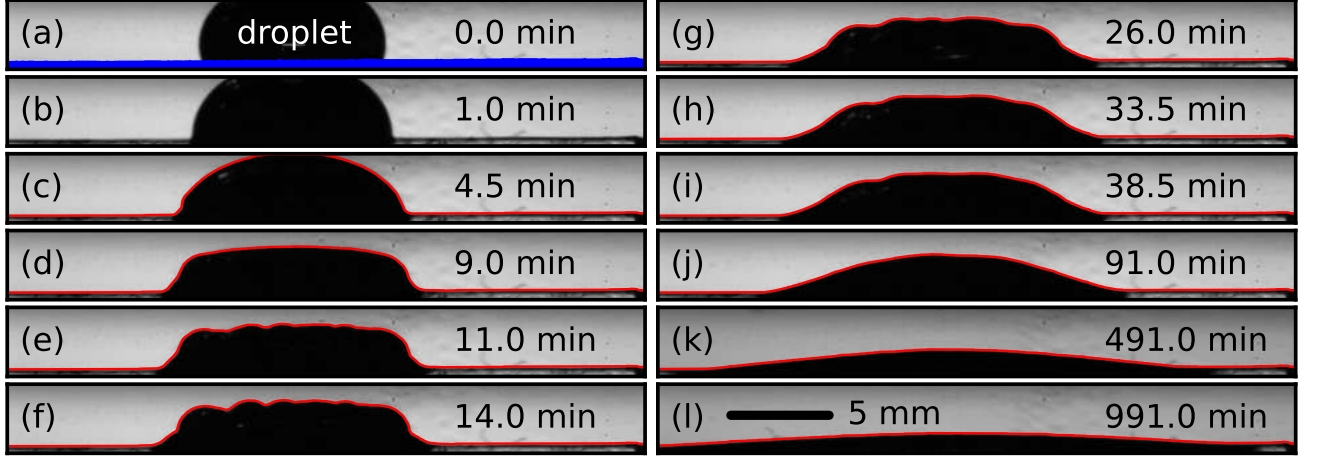


FIG. 2. Sequence of photographs showing the absorption of a 100 μl droplet into the hydrogel sheet. (a-d): States with liquid water remaining. (e-f): A surface instability forms. (f-h): Transition towards the long-time spreading regime which is shown in (h-l). The visible hydrogel sheet is marked blue in (a). From (c) onward a red line marks the hydrogel-oil interface.

where the hydrogel sheet permeability κ satisfies

$$\kappa = \kappa_0 \left(\frac{\phi_{0p}}{\phi_p} \right)^\beta. \quad (6)$$

Here κ_0 is the characteristic permeability scale while β is a parameter to be determined by fitting to experimental data (see [36] for further details). We exploit a shallow-water lubrication approximation, namely that the characteristic radial length scale the initial radius of the blister $R_0 = R(t=0)$ is much greater than the characteristic vertical length scale, the initial height $H_0 = h(r=0, t=0)$. We nondimensionalise the equations anisotropically using these length scales and define $\mathcal{P} = p/P_0$, $k = \kappa/\kappa_0$, such that

$$\rho = \frac{r}{R_0}, \quad \tau = \frac{U_0 t}{R_0}, \quad \mathcal{R} = \frac{R(t)}{R_0},$$

$$\mathcal{H} = \frac{h(r, t)}{H_0}, \quad \mathcal{A} = \frac{a}{H_0}, \quad \mathcal{V} = \frac{d^3}{12R_0^2 H_0},$$

where the characteristic velocity scale $U_0 = \kappa_0(K + 4G/3)/(R_0\mu_f)$ arises from the pressure gradients induced by the elastic stresses inherent in the polymer matrix. Keeping only leading-order terms in $\epsilon = H_0/R_0$ (see [36]), the model admits a vertically independent solution for the polymer volume fraction ϕ_p with corresponding elastic deformation vector ξ satisfying

$$\phi_p = \frac{\mathcal{A}}{\mathcal{H}} \phi_{0p}, \quad \xi = z \left(1 - \frac{\mathcal{A}}{\mathcal{H}} \right) e_z. \quad (7)$$

The deflection of the hydrogel surface $\overline{\mathcal{H}} = \mathcal{H} - \mathcal{A}$ satisfies a conservation law of the form $\partial \overline{\mathcal{H}} / \partial \tau = -\nabla \cdot \mathcal{J}_{\mathcal{H}}$,

$$\frac{\partial \overline{\mathcal{H}}}{\partial \tau} = \frac{1}{\rho} \frac{\partial}{\partial \rho} \left(\rho \left(\frac{\overline{\mathcal{H}} + \mathcal{A}}{\mathcal{A}} \right)^{\beta-1} \frac{\partial \mathcal{H}}{\partial \rho} \right), \quad (8)$$

in which the flux $\mathcal{J}_{\mathcal{H}} = -(1 + \overline{\mathcal{H}}/\mathcal{A})^{\beta-1} \nabla_\rho \mathcal{H}$ is a plug-flow Darcy law term, dominated by the radial pressure gradient, together with the volume conservation condition

$$\int_0^\infty \rho \overline{\mathcal{H}} d\rho = \mathcal{V}. \quad (9)$$

For general \mathcal{A} , (8) does not admit an analytic solution. Hence, we solve it numerically using the finite-element software package FEniCS ([42], [43], with further details in [36]). However, this system admits self-similar solutions

$$\mathcal{H}_s - \mathcal{A} = \frac{1}{\mathcal{R}_s^2} \exp \left(-\frac{(1-\mathcal{A})}{2\mathcal{V}} \frac{\rho^2}{\mathcal{R}_s^2} \right), \quad (10a)$$

$$\mathcal{H}_l - \mathcal{A} = \frac{(1-\mathcal{A})}{\mathcal{R}_l^2} \left(1 - \frac{(1-\mathcal{A})(\beta-1)}{2\beta\mathcal{V}} \frac{\rho^2}{\mathcal{R}_l^2} \right)^{1/(\beta-1)}, \quad (10b)$$

in the small ($\mathcal{H}_s, 1-\mathcal{A} \ll 1$) and the large ($\mathcal{H}_l, \mathcal{A} \ll 1$) deformation limit respectively, with

$$\mathcal{R}_s = \left(1 + \frac{2\tau(1-\mathcal{A})}{\mathcal{V}} \right)^{1/2}, \quad (11a)$$

$$\mathcal{R}_l = \left(1 + \frac{2\tau(1-\mathcal{A})^\beta \mathcal{A}^{\beta-1}}{\mathcal{V}} \right)^{1/(2\beta)}. \quad (11b)$$

We anticipate that the evolution of the blister will approach these similarity solutions asymptotically for large time, even when the initial conditions do not match the asymptotic form.

Figure 3 illustrates the time evolution of numerical solutions of (8) for \mathcal{R} for $\beta = 3/2$ and a range of values

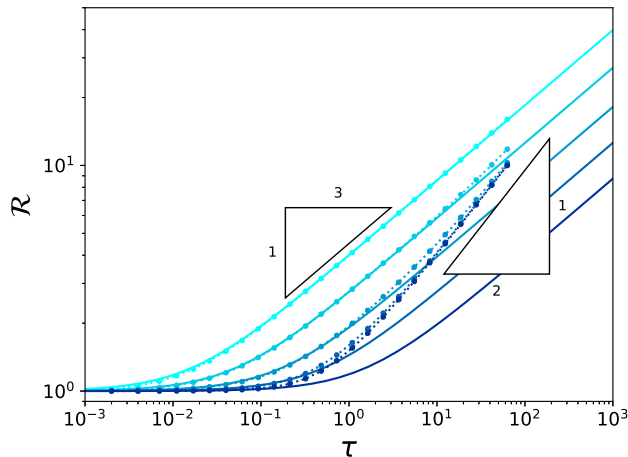


FIG. 3. Swelling dynamics of thin hydrogel sheets according to the proposed poroelastic model with an arbitrary choice of $\beta = 3/2$, $\mathcal{V} = 1 - \mathcal{A}$ and $\mathcal{A} \in [0.001, 0.01, 0.1, 0.5, 0.9]$ (light to dark blue) where darker colours denote larger \mathcal{A} . Dotted lines with circles plot the scaled blister radius $\mathcal{R} = R(t)/R(0)$ of numerical solutions of (8) as a function of time, using a self-similar initial height profile of the form given in (10b). For comparison, solid lines show the radius predicted by the self-similar solution in the large deformation limit (11b).

of \mathcal{A} (darker blue denotes larger \mathcal{A}). Dotted lines with circles denote numerical solutions of (8) evolved from an initial condition of the form given in (10b), where \mathcal{R} is defined as the radius at which the blister height has decreased to half of the maximum height (see fig 1 and SuppMat (S1, S35)). Solid lines denote the corresponding large deformation similarity solutions (11b). For large deformations, when both τ and \mathcal{A} are small, the large deformation similarity solution (11b) agrees well with \mathcal{R} obtained from the numerics, where $\mathcal{R} \sim \tau^{1/3}$. Since the maximum height of the blister $\max(\mathcal{H})$ decreases as time passes, the system eventually reaches the small deformation region with corresponding similarity solution given for \mathcal{R} in (11a), with $\mathcal{R} \sim \tau^{1/2}$.

Experimentally, $0.40 < \mathcal{A} < 0.68$ lies in the intermediate regime. This, together with the necessary resolution of a virtual origin problem, precludes a comprehensive direct quantitative test of the similarity solutions (which will describe the behaviour of the blister after an initial adjustment period) against our experimental data. Instead, we solve (8) numerically, using an experimentally observed initial condition. The initial conditions were obtained from the conditions at $t = t_0$, with t_0 selected separately for each experiment to ensure both that the model assumptions were justified and that any buckling instability had decayed. The numerical solutions predict the evolution of the blister as a function of dimensionless time τ with a single fitted parameter β . Hence, for each experiment the poroelastic time scale $\tau_0 = \mu_f R_0^2 / \kappa_0 (K + 4G/3)$ (where R_0 is different for

each experiment) has to be determined by globally fitting $\Omega = \tau_0 / R_0^2 = \mu / (\kappa_0 (K + 4G/3))$, since K , G and κ_0 are unknown for our hydrogel. We found $\Omega = 7.3 \times 10^9 \text{ s mm}^{-2}$ and $\beta = 2.16 \pm 0.083$ by a simultaneous fit to all data sets [36], leading to $\tau_0 = 4.50 - 40.86 \text{ h}$ since the initial radii vary considerably by almost a factor of three between the datasets. This large variation in time scale is due to the initial radius varying by almost a factor of three between the datasets. This fit is not particularly sensitive to β ; if we had chosen $\beta = 1.83$, the highest value reported in the literature cited [44], Ω would have decreased slightly to 109 min mm^{-2} .

Since our model neglects elastic deformation gradients in the z direction, we expect τ_0 to be much greater than the time scale on which these gradients decay. If we assume that the absence of the buckling instability after 30 min indicates the decay of vertical gradients, this is indeed the case.

Whilst $\beta = 2.16$ is considerably larger than the suggestion (2/3) made by one of the present authors [41], it appears to be compatible with previous experimental studies (1.5–1.84) [30, 44, 45].

Figure 4 compares experimental data (circles) with the corresponding numerical predictions (lines) generated using the theoretical model and the fitted parameters, taking initial conditions directly from the experimental data that they are fitted against (darker blue curves indicate larger initial droplets). Figure 4(a) explores how the maximum scaled blister height $\max(\mathcal{H})$ evolves temporally for different droplet volumes. A good agreement is found for all data sets for the full range of experimental data. Figure 4(b) compares the half-height radius of the blister obtained from experimental and numerical data. The numerical solutions capture the experimental trend very well. However, the accuracy of the numerical prediction varies. In particular for experiments with small droplets, the good agreement at early times breaks down at later times where the numerical solutions underpredict the blister radius. In contrast in experiments with large droplets, good agreement is observed over the full range of experimental data. The Supplementary Material [36] discusses how the dominant measurement error arises from imperfect alignment of the camera and the sample. This could introduce an error of $\delta h \approx 45 \mu\text{m}$, which we expect to affect the determination of \mathcal{R} strongly once $h(r, t) - a$ becomes small in the late stages of an experiment.

In conclusion, we believe these findings will aid the study of transient, highly localised swelling phenomena in hydrogels and related polymers. Our experiments demonstrate optical methods to generate imaging contrast of these inherently transparent systems and how to isolate transport within the polymer from the surrounding gas phase.

Rather than constructing a model for the hydrogel with a fully non-linear constitutive equation [25], we have

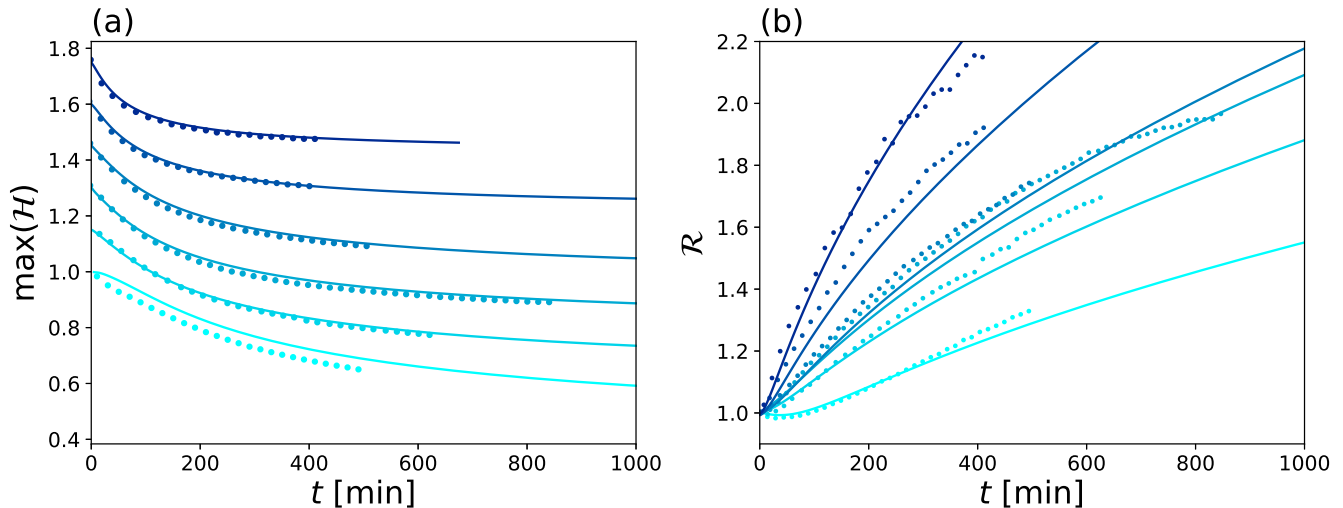


FIG. 4. The temporal evolution of the maximum scaled height $\max(\mathcal{H})$ (a) and the scaled radius \mathcal{R} (b) of the swelling region for a range of different initial droplet volumes, plotting experimental data with circles and numerical solutions with lines. Lighter blue curves correspond to larger initial droplet volumes. For clarity in (a), each data set for $\max(\mathcal{H})$ is shown with an offset of 0.15. Numerical solutions are generated using initial conditions taken directly from the experimental data that they are fitted against.

demonstrated the efficacy of a linear poroelastic equation for σ combined with non-linear kinematic equations. Despite being outside the formal validity range of linear elasticity, this approach is common within poroelasticity research to obtain simplified models for finite deformation [46]. Linear poroelastic models have a rigorous relationship with the aforementioned non-linear models [22, 26]. They avoid the hidden problems inherent in non-linear models arising from the limited extensibility of the polymer chains that mean that for highly-swollen gels it is necessary to use non-Gaussian statistics to model the changes in entropy due to mechanical stretching [24].

We demonstrate that, in the lubrication limit, our fully three-dimensional model reduces to a single one-dimensional non-linear diffusion equation for the evolution of the non-dimensional height of the layer \mathcal{H} . This key insight extends the geometries potentially amenable to analytical treatment beyond strictly one-dimensional geometries [3, 29, 30].

Importantly, our approach establishes an experimental and theoretical connection between the polymer swelling literature and a large body of work considering spreading in thin porous layers [47–50]. This will accelerate further progress for complex swelling problems in slender geometries, where the polymer interacts with its environment in complex fashion. Examples are the absorption of droplets [31], mass transfer between a shear flows and swelling polymer surfaces [51] (see Landel *et al.* [52] for a non-swelling example) and the growth of biofilms on tissue [53].

ACKNOWLEDGEMENTS

The authors would like to thank the late Dr Henry McEvoy (Dstl, Porton Down) and Professor M. Grae Worster (Cambridge) for proposing the problem. The authors thank Dr Steve Marriott (Dstl, Porton Down) for his help with the Karl-Fischer titration and MGW for his comments on the manuscript. MAE, JRL and SBD acknowledge funding from Dstl under extramural research agreement DSTLX-1000138254. GTF acknowledges a Doctoral Training Fellowship from the Engineering and Physical Sciences Research Council.

-
- [1] W. A. Laftah, S. Hashim, and A. N. Ibrahim, Polymer hydrogels: A review, *Polymer-Plastics Technology and Engineering* **50**, 1475 (2011).
 - [2] S. Vervoort, *Behaviour of hydrogels swollen in polymer solutions under mechanical action.*, Ph.D. thesis, École Nationale Supérieure des Mines de Paris, France (2006).
 - [3] J. Yoon, S. Cai, Z. Suo, and R. C. Hayward, Poroelastic swelling kinetics of thin hydrogel layers: comparison of theory and experiment, *Soft Matter* **6**, 6004 (2010).
 - [4] S. Tortorella, G. Inzalaco, F. Dapporto, M. Maturi, L. Sambri, V. V. Buratti, M. Chiariello, M. C. Franchini, and E. Locatelli, Biocompatible pectin-based hybrid hydrogels for tissue engineering applications, *New J. Chem.* **45**, 22386 (2021).
 - [5] B. Ozcelik, Degradable hydrogel systems for biomedical applications, in *Biosynthetic Polymers for Medical Applications*, edited by L. Poole-Warren, P. Martens, and R. Green (Elsevier, 2016) pp. 172–188.

- [6] A. Richter, S. Klatt, G. Paschew, and C. Klenke, Micropumps operated by swelling and shrinking of temperature-sensitive hydrogels, *Lab on a Chip* **9**, 613 (2009).
- [7] G. H. Kwon, G. S. Jeong, J. Y. Park, J. H. Moon, and S.-H. Lee, A low-energy-consumption electroactive valveless hydrogel micropump for long-term biomedical applications, *Lab on a Chip* **11**, 2910 (2011).
- [8] L. Ionov, Hydrogel-based actuators: possibilities and limitations, *Materials Today* **17**, 494 (2014).
- [9] T. Porter, R. Stewart, J. Reed, and K. Morton, Models of hydrogel swelling with applications to hydration sensing, *Sensors* **7**, 1980 (2007).
- [10] A. S. Hoffman, Hydrogels for biomedical applications, *Advanced drug delivery reviews* **64**, 18 (2012).
- [11] O. Wichterle and D. Lim, Hydrophilic gels for biological use, *Nature* **185**, 117 (1960).
- [12] J. L. Drury and D. J. Mooney, Hydrogels for tissue engineering: scaffold design variables and applications., *Biomaterials* **24**, 4337 (2003).
- [13] A. S. Hoffman, Hydrogels for biomedical applications, *Adv. Drug Deliv. Rev.* **64**, 18 (2012).
- [14] C. Walsh, E. Stride, U. Cheema, and N. Ovenden, A combined three-dimensional in vitro - in silico approach to modelling bubble dynamics in decompression sickness, *J. R. Soc. Interface* **14**, 20170653 (2017).
- [15] Y. Zhang, M. A. Etzold, and A. Lefauve, Growth of gas-filled penny-shaped cracks in decompressed hydrogels, *Soft Matter* **17**, 815 (2021).
- [16] K. Y. Lee and D. J. Mooney, Hydrogels for tissue engineering, *Chem. Rev.* **101**, 1869 (2001).
- [17] G. Tang, B. Zhou, F. Li, W. Wang, Y. Liu, X. Wang, C. Liu, and X. Ye, Advances of naturally derived and synthetic hydrogels for intervertebral disk regeneration, *Frontiers in Bioengineering and Biotechnology* **8**, 745 (2020).
- [18] P. Madhusudanan, G. Raju, and S. Shankarappa, Hydrogel systems and their role in neural tissue engineering, *J. R. Soc. interface* **17**, 20190505 (2020).
- [19] P. Deng, L. Yao, J. Chen, Z. Tang, and J. Zhou, Chitosan-based hydrogels with injectable, self-healing and antibacterial properties for wound healing, *Carbohydrate Polymers* **276**, 118718 (2022).
- [20] B. Stubbe, A. Mignon, L. V. Damme, K. Claes, H. Hoeksema, S. Monstry, S. V. Vlierberghe, and P. Dubruel, Photo-crosslinked gelatin-based hydrogel films to support wound healing, *Macromol. Biosci.* **21**, 2100246 (2021).
- [21] A. Cont, T. Rossy, Z. Al-Mayyah, and A. Persat, Biofilms deform soft surfaces and disrupt epithelia, *eLife* , 9:e56533 (2020).
- [22] M. Doi, Gel dynamics, *Journal of the Physical Society of Japan* **78**, 052001 (2009).
- [23] W. Hong, X. Zhao, J. Zhou, and Z. Suo, A theory of coupled diffusion and large deformation in polymeric gels, *Journal of the Mechanics and Physics of Solids* **56**, 1779 (2008).
- [24] S. A. Chester and L. Anand, A coupled theory of fluid permeation and large deformations for elastomeric materials, *Journal of the Mechanics and Physics of Solids* **58**, 1879 (2010).
- [25] S. Cai and Z. Suo, Equations of state for ideal elastomeric gels, *EPL (Europhysics Letters)* **97**, 34009 (2012).
- [26] N. Bouklas and R. Huang, Swelling kinetics of polymer gels: comparison of linear and nonlinear theories, *Soft Matter* **8**, 8194 (2012).
- [27] P. Van de Velde, S. Protière, and C. Duprat, Dynamics of drop absorption by a swelling fiber, *Soft Matter* **17**, 6168 (2021).
- [28] T. Tanaka and D. J. Fillmore, Kinetics of swelling of gels, *The Journal of Chemical Physics* **70**, 1214 (1979).
- [29] M. Engelsberg and W. Barros Jr, Free-evolution kinetics in a high-swelling polymeric hydrogel, *Physical Review E* **88**, 062602 (2013).
- [30] T. Bertrand, J. Peixinho, S. Mukhopadhyay, and C. MacMinn, Dynamics of swelling and drying in a spherical gel, *Phys. Rev. Applied* **6**, 064010 (2016).
- [31] A. Phadnis, K. C. Manning, I. Sanders, T. P. Burgin, and K. Rykaczewski, Droplet-train induced spatiotemporal swelling regimes in elastomers, *Soft Matter* **14**, 5869 (2018).
- [32] C. Yu, K. Malakpoor, and J. M. Huyghe, Comparing mixed hybrid finite element method with standard fem in swelling simulations involving extremely large deformations, *Computational Mechanics* **66**, 287 (2020).
- [33] R. Li, Y. Shi, M. Alsaedi, M. Wu, L. Shi, and P. Wang, Hybrid hydrogel with high water vapor harvesting capacity for deployable solar-driven atmospheric water generator, *Environmental Science & Technology* **52**, 11367 (2018), pMID: 30192516.
- [34] M. J. Varady, T. P. Pearl, S. M. Stevenson, and B. A. Mantooth, Decontamination of vx from silicone: characterization of multicomponent diffusion effects, *Industrial & Engineering Chemistry Research* **55**, 3139 (2016).
- [35] D. R. Hewitt, J. S. Nijjer, M. G. Worster, and J. A. Neufeld, Flow-induced compaction of a deformable porous medium, *Phys. Rev. E* **93**, 023116 (2016).
- [36] See Supplemental Material at <http://link.aps.org/supplemental/10.1103/XXX> for further theoretical details and experimental methods.
- [37] S. Van der Walt, J. L. Schönberger, J. Nunez-Iglesias, F. Boulogne, J. D. Warner, N. Yager, E. Gouillart, and T. Yu, scikit-image: image processing in python, *PeerJ* **2**, e453 (2014).
- [38] C. R. Harris, K. J. Millman, S. J. van der Walt, R. Gommers, P. Virtanen, D. Cournapeau, E. Wieser, J. Taylor, S. Berg, N. J. Smith, R. Kern, M. Picus, S. Hoyer, M. H. van Kerkwijk, M. Brett, A. Haldane, J. F. del Río, M. Wiebe, P. Peterson, P. Gérard-Marchant, K. Sheppard, T. Reddy, W. Weckesser, H. Abbasi, C. Gohlke, and T. E. Oliphant, Array programming with NumPy, *Nature* **585**, 357 (2020).
- [39] A. Onuki, Pattern formation in gels, *Journal of the Physical Society of Japan* **57**, 703 (1988).
- [40] N. Bouklas, C. M. Landis, and R. Huang, A nonlinear, transient finite element method for coupled solvent diffusion and large deformation of hydrogels, *Journal of the Mechanics and Physics of Solids* **79**, 21 (2015).
- [41] M. A. Etzold, P. Linden, and M. G. Worster, Transpiration through hydrogels, *Journal of Fluid Mechanics* **925** (2021).
- [42] M. S. Alnæs, J. Blechta, J. Hake, A. Johansson, B. Kehlet, A. Logg, C. Richardson, J. Ring, M. E. Rognes, and G. N. Wells, The fenics project version 1.5, *Archive of Numerical Software* **3**, 10.11588/ans.2015.100.20553 (2015).
- [43] A. Logg, K.-A. Mardal, G. N. Wells, *et al.*, *Automated Solution of Differential Equations by the Finite Element* (Springer, 2012).

- [44] C. A. Grattoni, H. H. Al-Sharji, C. Yang, A. H. Mugeridge, and R. W. Zimmerman, Rheology and permeability of crosslinked polyacrylamide gel, *Journal of colloid and interface science* **240**, 601 (2001).
- [45] M. Tokita and T. Tanaka, Friction coefficient of polymer networks of gels, *The Journal of chemical physics* **95**, 4613 (1991).
- [46] C. W. MacMinn, E. R. Dufresne, and J. S. Wettlaufer, Fluid-driven deformation of a soft granular material, *Phys. Rev. X* **5**, 011020 (2015).
- [47] O. M. Phillips, *Geological Fluid Dynamics: Sub-surface Flow and Reactions* (Cambridge University Press, 2009).
- [48] D. R. Hewitt, J. A. Neufeld, and N. J. Balmforth, Shallow, gravity-driven flow in a poro-elastic layer, *J. Fluid Mech.* **778**, 335 (2015).
- [49] J. M. Nordbotten and M. A. Celia, Similarity solutions for fluid injection into confined aquifers, *J. Fluid Mech.* **561**, 307 (2006).
- [50] J. Rutqvist, The geomechanics of co2 storage in deep sedimentary formations, *Geotech. Geol. Engng* **30**, 525 (2012).
- [51] J. Delavoipière, B. Heurtefeu, J. Teisseire, A. Chateauminois, Y. Tran, M. Fermigier, and E. Verneuil, Swelling dynamics of surface-attached hydrogel thin films in vapor flows, *Langmuir* **34**, 15238 (2018).
- [52] J. R. Landel, A. Thomas, H. McEvoy, and S. B. Dalziel, Convective mass transfer from a submerged drop in a thin falling film, *Journal of Fluid Mechanics* **789**, 630 (2016).
- [53] G. T. Fortune, N. M. Oliveira, and R. E. Goldstein, Biofilm growth under elastic confinement, arXiv:2112.02540 [cond-mat.soft] (2022).

Droplet absorption into thin layers of polymer: Supplementary Material

Merlin A. Etzold¹, George T. Fortune¹, Julien R. Landel² and Stuart B. Dalziel¹

¹*Department of Applied Mathematics and Theoretical Physics,
Centre for Mathematical Sciences, University of Cambridge,
Wilberforce Road, Cambridge CB3 0WA, United Kingdom*

²*Department of Mathematics, Alan Turing Building,
University of Manchester, Oxford Road, Manchester, M13 9PL, UK*

(Dated: February 22, 2022)

EXPERIMENTAL

Supplementary information on methods and materials

We used commercially available medical grade hydrogel pads (Hydrogel Nipple Pads, Medela, Switzerland), which were manufactured as approximately $8 \times 8 \text{ cm}^2$ -sheets. The hydrogel pads appear as a rubbery sheet with a slightly tacky surface. After prolonged exposure to the atmosphere (ca. 25-40% relative humidity, ca. 22°C), their initial thickness was determined with a micrometer as $a_0 = 1.13 \text{ mm} \pm 0.01 \text{ mm}$. One side of a sheet was affixed to a thin plastic sheet (impermeable to water) of approximate thickness 0.04 mm. The other side was initially protected by an easily removable plastic film. The hydrogel sheets incorporate a thin gauze during their manufacture, probably to provide mechanical coherence/strength in the plane of the sheet, but this gauze did not appear to affect the swelling of the sheets. In our experiments, these larger sheets were cut into approximately $25 \times 25 \text{ mm}^2$ -coupons. The coupons were then glued (via the thin impermeable plastic film) onto $76 \times 26 \text{ mm}^2$ microscope slides (Menzel, Germany) with UV-cured Norland Optical Adhesive NOA 68 optical glue (Thorlabs, USA).

Utilising Karl-Fischer titration (KFT), the water content of a typical hydrogel pad that had equilibrated with the laboratory air was measured to be 22%. We found that isopropanol and ethanol did not swell the hydrogel perceptively. When placed in saturated sodium chloride solutions the swelling was drastically reduced. We take these observations as evidence for the presence of charged groups within the hydrogel.

Imaging system

A monochrome camera (SP-5000M-CXP2, Jai, Denmark) with a variable magnification telecentric lens (TEV0305, VS Technology Corporation, Japan, utilising $0.4\times$ magnification) aligned with the hydrogel plane, observed the evolution of our samples. Background lighting was provided by a white LED light sheet (MiniSun Light Pad 17031) masked with black tape and placed

approximately 4 m away from the hydrogel to ensure approximately collimated illumination (see figure 1(a) in the main text for a schematic of this setup).

Digiflow was used for camera control [S1] and captured images were analysed using a Canny edge detector from the Scikit Image Library [S2] in Python. Suitable parameters for the edge detector (radius of Gaussian filter, upper and lower gradient thresholds for edge detection) were manually set for each dataset using a custom interactive interface.

Suppression of vapour transport

In preliminary experiments, water droplets were placed onto mounted hydrogel that was otherwise exposed to air but enclosed into a sealed cell to prevent evaporation into the atmosphere (the imaging system was similar to the present setup shown in the main text in figure 1(a)). The edges of the hydrogel sheet were observed to swell perceptively, with the swelling beginning immediately after droplet placement. This was attributed to evaporation from the strongly swollen regions (the regions in the vicinity of the droplet) leading to humidity gradients in the sealed cell and thus reabsorption by the drier regions of the hydrogel at the edge of the sheet. This was confirmed by experiments in which water droplets were placed next to the hydrogel on separate microscope slides within the sealed cell; swelling was still observed which could have only have come from vapour phase transport.

To eliminate vapour transport experimentally, the hydrogel was immersed in a water-immiscible oil (CASTROL HySpin AWS 32). Since even apparently immiscible liquids are sparingly soluble into each other, we confirmed the water content of the hydraulic to be 6700 ppm after prolonged exposure to the laboratory air using KFT. We also conducted a KFT with oil that had been equilibrated with a small amount of water, indicating an estimate for the equilibrium water content of the oil to be up to 1.1%, however, this might be an overestimation due to emulsion formation during shipping of the oil-water mixture to the place of analysis. To make sure that the oil and the hydrogel would be in equilibrium, they were both exposed to the same atmosphere before the experiment for at least 2 d; the oil was not changed between experiments and thus was always exposed to the

atmosphere. Furthermore, the hydrogel sheets were allowed to equilibrate for at least 1–3 h within the oil before droplet placement.

Characteristic radius and conservation of volume

As indicated in figure 1(b) of the main text, we extract a characteristic radius of the blister from experimental and numerical profiles (see also (S36) below) as the radius at which the blister height $h(r, t) - a$ has decreased from the maximum height of the blister $\max(h(\tilde{r})) - a$ to half of this value, thus

$$R = \left\{ r : h(r) - a = \frac{1}{2} \left(\max_{\tilde{r}}(h(\tilde{r})) - a \right) \right\}. \quad (\text{S1})$$

Figure I(b) plots the extracted raw data for the radius of the swollen region R , spanning the complete duration of an experiment from the moment that the droplet makes contact with the hydrogel surface. Initially, R sharply increases as the water droplet, having made contact, spreads slightly over the surface of the hydrogel (see figure 2(a) in the main text). Next, R decreases slightly, as the morphology of the blister changes from being a relatively flat-capped shape, caused by the horizontal redistribution of water above the droplet as it is absorbed at a rate that is nearly constant over the entire droplet radius, towards a smoother more self-similar shape (see figures 2(b) to 2(h) in the main text). Finally, we reach a regime where the radius of the swollen region increases monotonically (see figures 2(i) to 2(l) in the main text).

Assuming axisymmetry, an estimate for the volume of the blister was obtained by integrating the height profile obtained from the side view camera. This was plotted as a function of time in Figure I(a) where the nominal volume of the data set is shown as a horizontal dotted line while full lines map how the volume of the swollen region temporally evolves for the different experiments. In all experiments, the initial volume is overestimated. This is attributed to the initial creasing of the surface of the hydrogel. Only the silhouette of the external envelop is visible to the side-view camera, hiding the surface depressions associated with the creasing, and thus the creases would not be accounted for in the image processing integration step. For large droplets, the volume decreases approximately linearly in time. This is in stark contrast to the smaller droplets where the volume appears to be nearly constant.

A key modelling assumption that we make is to assume local water volume conservation, from which it follows that the total blister volume should be conserved during the experiment. Our diagnostics indicates a loss of volume across the duration of an experiment, in particular for experiments with larger droplets. Below, we thus investigate mass transfer from the water droplet into the

oil and find that it can be neglected. Our analysis of systematic errors in the imaging system shows that misalignment of hydrogel and camera can lead to the inability of the camera to detect small swelling that is hidden below the edge of the hydrogel. This can indeed explain the correct order of magnitude to explain the experimentally observed volume loss and hence validates volume conservation as a reasonable modelling assumption to make.

CONSERVATION OF WATER VOLUME

Volume loss estimate through mass transport into or through the oil

One explanation for a loss of water volume in the hydrogel is mass transport across the interface into the oil layer. Since there is a sparse solubility of water in the hydraulic oil (see above), we investigated the water losses due to transport in the oil phase. Here, we make an order of magnitude estimation for the volume loss from this transport by considering the effect from diffusive mass flux in the z -direction. We assume that mass flux is due to diffusion only (no advective component) and that the oil is saturated with water at the interface to the hydrogel swollen region (estimated to be 1.1 % water content, which is an overestimation since the chemical potential of water in unsaturated hydrogel is less than pure water Etzold *et al.* [S3]) and is in equilibrium with the laboratory atmosphere far away from the hydrogel (estimated to be 0.67 % water content). Hence, we estimate the difference in water volume concentration Δc that drives diffusion as

$$\Delta c \approx \Delta \omega \rho_o, \quad (\text{S2})$$

where the difference in water mass fraction that drives diffusion $\Delta \omega = 0.43\%$, the density of mineral oil $\rho_o = 833 \text{ kg m}^{-3}$ and we have assumed both ideal mixing and that the water concentration in the oil is small. At a fixed radial distance $r = r'$, the concentration field $c = c(r', z, t, t')$ can be described using the similarity solution for the one-dimensional diffusion equation in Cartesian coordinates,

$$c = \Delta c \operatorname{erfc}(z/\sqrt{4D(t-t')}), \quad (\text{S3a})$$

with corresponding diffusive water mass flux

$$j = \frac{\Delta c \sqrt{D}}{\sqrt{\pi(t-t')}}, \quad (\text{S3b})$$

where erfc is the complementary error function, D is the water diffusion coefficient and t' is the time at which the swelling front reaches r' ($r' = R(t')$). The total water volume lost for a swollen blister thus becomes

$$\Delta V = \frac{1}{\rho_w} \int_0^t \left[A_0 j(t') + \frac{\partial A}{\partial t}(t') \otimes j(t') \right] dt', \quad (\text{S4})$$

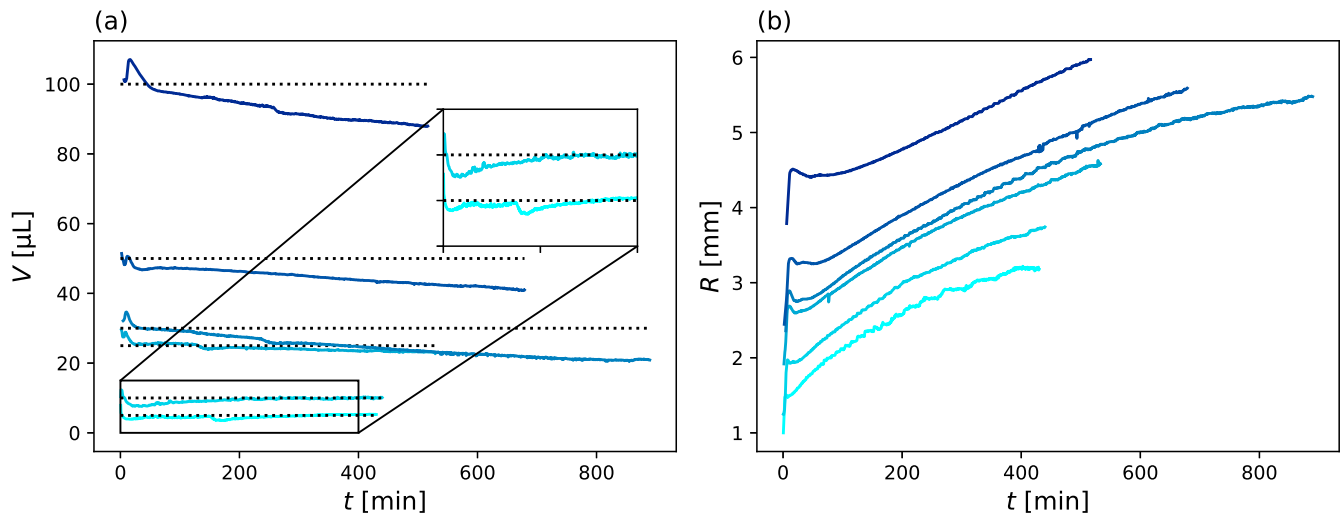


FIG. I. Raw data showing for a range of experiments how in (a) the apparent volume of the blister (found by direct integration) and in (b) the radius of the swollen region vary as functions of time. Darker blue curves denote experiments with larger water droplets.

where we have assumed that the blister has a circular base and surface area $A(t)$ with $A(0) = A_0$. The convolution integral denoted by \otimes accounts for the fact that diffusion starts only when the hydrogel starts to swell. Assuming the radius to grow linearly with growth rate χ , namely $A(t) = \pi(R_0 + \chi t)^2$, this simplifies to become

$$\begin{aligned} \Delta V &= \frac{2\rho_o}{\rho_w} \sqrt{\pi D} \Delta\omega \left[R_0^2 \sqrt{t} + \int_0^t \int_0^{t'} \chi \frac{(R_0 + \chi t'')}{\sqrt{t' - t''}} dt'' dt' \right] \\ &= \frac{2\rho_o}{\rho_w} \sqrt{\pi D} \Delta\omega \left[R_0^2 \sqrt{t} + \frac{4}{15} \chi t^{3/2} (5R_0 + 2\chi t) \right]. \end{aligned} \quad (\text{S5})$$

Utilising the experimental data for the largest blister (see figure I and table i) with initial radius $R_0 = 5$ mm, approximating the radius as growing linearly with time yields an effective $\chi = 0.5$ mm h⁻¹. We found no water diffusion data for the oil and established that such data is not widely available for mineral oils. However, given its relatively high viscosity of $\mu_o = 32$ cSt at 40 °C the water diffusion coefficient in oil is likely to be an order of magnitude less than the self diffusion coefficient of water, $D = 3 \times 10^{-9}$ m² s⁻¹. Furthermore, Hilder and van den Tempel reported water diffusion coefficients for groundnut oil (50 times more viscous than water) and kerosene (twice as viscous as water) as 2.5×10^{-10} m² s⁻¹ and 8.5×10^{-10} m² s⁻¹ respectively [S4]. Hence, taking the diffusion constants for groundnut oil and kerosene as lower and upper bounds respectively for the diffusion constant of our hydraulic oil, (S5) predicts diffusive volume losses of {0.3 – 0.6}, {1.2 – 2.2}, and {2.7 – 5.0} μ l after one, five and ten hours respectively. As this is an order of magnitude too small to account for the volume loss found in Figure I(a), we must look elsewhere.

For completeness, a supplementary experiment was conducted where a 2 μ l droplet of water was placed directly onto a microscope slide immersed into an oil bath with no hydrogel present. This droplet reached a sessile state after 25 h. Whilst the accuracy of our image analysis of this experiment was impacted from resolution issues in locating the diffuse edges of the droplet, we found that the water loss of the droplet was less than 0.1 μ l over a time period of approximately 120 h. Its surface area remained approximately constant and was estimated to be 4.6 mm². Assuming a steady state mass loss from the droplet into the atmosphere through a 1 cm deep layer of oil yields a diffusion coefficient of $1\text{-}2 \times 10^{-10}$ m² s⁻¹. By approximating this curved diffusion problem using the equations above, assuming mass transport into an infinite oil bath yields an even lower diffusion coefficient of 7×10^{-11} m² s⁻¹.

In conclusion, based on diffusion coefficients in the literature for water in oil, it is unlikely that the swollen hydrogel loses a significant amount of water into the oil during the duration of an experiment. This is corroborated by a supplementary experiment testing the stability of a small water droplet in the same conditions.

Errors in the imaging system

An alternative explanation for the apparent volume loss in experiments with large droplets are the uncertainties inherent when capturing the evolution of the system using the side view camera, leading to measurement errors δr and δz in the radial and vertical directions respectively. We assume that the camera is able to pick up the position of the surface with an accuracy of within one

pixel. With a pixel pitch of $5\ \mu\text{m}$ at 0.4 magnification, this corresponds to a measurement error in horizontal and vertical direction of $\delta z = \delta r = 12.5\ \mu\text{m}$.

However, when finding an order of magnitude estimate for the error in determining $h(r, t)$, δz , the finite size of pixels is not the main source of error since $h(r, t)$ is not measured directly. Instead, we measure the difference between the highest swollen point of a parallel projection of the hydrogel and the height of the projection of the unswollen gel, $h(r, t) - a$, by comparing the projected upper edge of the hydrogel in the swollen state with the upper edge of the hydrogel in the unswollen state (see figures 1 and 2 in the main text). This introduces errors arising from the imperfect alignment between the camera and the sample. Due to a combination of manufacturing imperfections and the variations in the process of gluing the sample to the microscope slides, the open surface of the hydrogel coupons is not completely flat. This means that some swelling is invisible below the camera horizon, leading to an underestimation of the local swelling height and thus R and V . This is a systematic error within each experiment, but stochastic between different experiments. Assuming a misalignment of up to $\pm 0.1^\circ$ over the typical width of a hydrogel coupon $25\ \text{mm}$ corresponds to a vertical measurement error of $\delta h = 45\ \mu\text{m}$. This is significantly greater than δr .

For the $100\ \mu\text{l}$ droplet, this vertical uncertainty δz corresponds to a hidden volume of $3.5\ \mu\text{l}$ at the start of the experiment (assuming an initial swelling region of radius $5\ \text{mm}$) which increases to $14\ \mu\text{l}$ by the end of the experiment (assuming a final swelling region of radius $10\ \text{mm}$). This matches the experimental observed mass loss plotted in the top curve of figure I(a) very well. Hence, from this analysis, we can conclude that the hidden volume arising from imperfect alignment is the correct order of magnitude to explain the experimentally observed volume loss for experiments with large droplets.

POROELASTIC MODEL

Modelling the permeability of hydrogel

We model the dimensionless effective hydrogel permeability $k = \kappa/\kappa_0$ as an explicit dimensionless function of the polymer volume fraction ϕ_p . Since the true structure of these materials at the pore scale is complicated and unknown for our particular sample, this can only be an approximation. In the porous media literature, many different models for the concentration-dependence of κ have been used. In a geophysical context, Hewitt *et al.* [S5] for mathematical simplicity took the permeability of a shallow deformable porous layer as $k = 1$. Modelling bacterial biofilms, Seminara *et al.* [S6] set the permeability of a growing biofilm as $k = (1 - \phi)^2$ while Fortune *et al.* [S7] constructed the system in such a way to not

have to explicitly define k . When considering a spherical hydrogel, Bertrand *et al.* [S8] proposed $k = (1 - \phi_p)/\phi_p^\beta$. In the interest of simplicity we follow Tokita & Tanaka [S9] and Etzold *et al.* [S3] by defining

$$k = \left(\frac{\phi_{0p}}{\phi_p} \right)^\beta, \quad (\text{S6})$$

where β is a free parameter chosen by matching to experimental data. For a purely cuboidal network $\beta = 2/3$, but experiments have suggested values between $\beta = 1.5$ [S9] and 1.85 [S10].

Dimensionless shallow-layer scalings

We scale radial and vertical lengths with the initial radius $R_0 = R(t = 0)$ and height $H_0 = h(r = 0, t = 0)$ of the blister respectively i.e. $\{r, R\} \sim R_0$ and $\{z, h\} \sim H_0$. Since the characteristic time scale for the system is the poroelastic time scale for pressure driven fluid flow in the horizontal direction, we scale $t \sim \tau_0$ where

$$\tau_0 = \frac{\mu_f R_0^2}{(K + 4G/3)\kappa_0}. \quad (\text{S7})$$

From (1) of the main text, we have $u_f \sim U_0 = R_0/\tau_0$ and $\{w_f, w_p\} \sim H_0/\tau_0$. As horizontal and vertical elastic stresses in the hydrogel are of the same magnitude, $u_p \sim w_p \sim H_0/\tau_0$. Since \mathbf{u}_s is defined as the material derivative of $\boldsymbol{\xi}$, we have $\{\zeta, \xi\} \sim H_0$. By definition $\kappa \sim \kappa_0$. (4) of the main text implies that $\{p, \tilde{p}\} \sim P_0 = K + 4G/3$. Finally $d \sim (12R_0^2 H_0)^{1/3}$.

Non-dimensional Governing Equations

We now exploit a lubrication approximation, namely that the characteristic radial length scale R_0 is much greater than the characteristic vertical length scale H_0 . We nondimensionalise the dimensional governing equations given in the main text anisotropically using the scalings given above, denoting the dimensionless form of a function f by f^* and setting

$$\rho = \frac{r}{R_0}, \quad \tau = \frac{t}{\tau_0}, \quad \mathcal{H} = \frac{h(r, t)}{H_0}, \quad \mathcal{R} = \frac{R(t)}{R_0},$$

$$\mathcal{P} = \frac{p}{P_0}, \quad k = \frac{\kappa}{\kappa_0}, \quad \mathcal{A} = \frac{a}{H_0}, \quad \mathcal{V} = \frac{d^3}{12R_0^2 H_0}.$$

Keeping only leading-order terms in the aspect ratio $\epsilon = H_0/R_0 \ll 1$, the system of equations (1)-(4) in the main

text becomes

$$\frac{\partial \phi_p}{\partial \tau} + \frac{\partial}{\partial z^*} (\phi_p w_p^*) = \mathcal{O}(\epsilon), \quad (\text{S8a})$$

$$-\frac{\partial \phi_p}{\partial \tau} + \frac{\partial}{\partial z^*} ((1 - \phi_p) w_f^*) + \frac{1}{\rho} \frac{\partial}{\partial \rho} (\rho (1 - \phi_p) u_f^*) = 0, \quad (\text{S8b})$$

$$w_f^* - w_p^* = -\frac{k}{\epsilon^2 (1 - \phi_p)} \frac{\partial \mathcal{P}}{\partial z^*}, \quad (\text{S8c})$$

$$u_f = -\frac{k}{(1 - \phi_p)} \frac{\partial \mathcal{P}}{\partial \rho} + \mathcal{O}(\epsilon), \quad (\text{S8d})$$

$$\frac{\partial \mathcal{P}}{\partial \rho} = \frac{1}{\epsilon} \left(\frac{G}{K + 4G/3} \right) \frac{\partial^2 \xi^*}{\partial z^{*2}} + \left(\frac{K + G/3}{K + 4G/3} \right) \frac{\partial^2 \zeta^*}{\partial \rho \partial z^*} + \mathcal{O}(\epsilon), \quad (\text{S8e})$$

$$\frac{\partial \mathcal{P}}{\partial z^*} = \frac{\partial^2 \zeta^*}{\partial z^{*2}} + \epsilon \left(\frac{K + G/3}{K + 4G/3} \right) \frac{1}{\rho} \frac{\partial}{\partial \rho} \left(\rho \frac{\partial \xi^*}{\partial z^*} \right) + \mathcal{O}(\epsilon^2), \quad (\text{S8f})$$

where

$$u_p^* = \frac{\partial \xi^*}{\partial \tau} + w_p^* \frac{\partial \xi^*}{\partial z^*} + \mathcal{O}(\epsilon), \quad (\text{S8g})$$

$$u_p^* = \left(1 - \frac{\partial \zeta^*}{\partial z^*} \right)^{-1} \frac{\partial \zeta^*}{\partial \tau} + \mathcal{O}(\epsilon). \quad (\text{S8h})$$

Boundary conditions

The bottom of the hydrogel layer is glued to an impermeable rigid glass slide, meaning

$$w_f^* = 0 \text{ and } \xi^* = \zeta^* = 0 \implies u_p^* = w_p^* = 0 \text{ at } z^* = 0. \quad (\text{S9a})$$

The kinematic boundary conditions at the upper surface $z^* = \mathcal{H}$ are

$$w_p^* \Big|_{\mathcal{H}} = \frac{\partial \mathcal{H}}{\partial \tau} + \epsilon u_p^* \Big|_{\mathcal{H}} \frac{\partial \mathcal{H}}{\partial \rho}, \quad (\text{S9b})$$

$$w_f^* \Big|_{\mathcal{H}} = \frac{\partial \mathcal{H}}{\partial \tau} + u_f^* \Big|_{\mathcal{H}} \frac{\partial \mathcal{H}}{\partial \rho}. \quad (\text{S9c})$$

Vertically integrating (S8a) and then applying (S9) gives the polymer volume conservation condition

$$\frac{\partial}{\partial \tau} \left(\int_0^{\mathcal{H}} \phi_p dz^* \right) = -\epsilon (\phi_p u_p^*) \Big|_{\mathcal{H}} \frac{\partial \mathcal{H}}{\partial \rho}. \quad (\text{S9d})$$

The stress-free boundary at $z^* = \mathcal{H}$ gives

$$(\sigma^*)_{\rho z^*} \Big|_{\mathcal{H}} = 0 \implies \frac{\partial \xi^*}{\partial z^*} \Big|_{\mathcal{H}} = 0 + \mathcal{O}(\epsilon), \quad (\text{S9e})$$

$$\begin{aligned} (\mathcal{P} - (\sigma^*)_{z^* z^*}) \Big|_{\mathcal{H}^-} &= \mathcal{P} \Big|_{\mathcal{H}^-} - \frac{\partial \zeta^*}{\partial z^*} \Big|_{\mathcal{H}^-} + \mathcal{O}(\epsilon) \\ &= \mathcal{P} \Big|_{\mathcal{H}^+} = \mathcal{P}_0. \end{aligned} \quad (\text{S9f})$$

Global water conservation yields

$$\int_0^{\infty} \rho (\mathcal{H} - \mathcal{A}) d\rho = \mathcal{V}. \quad (\text{S9g})$$

Finally, in the far field the polymer in the hydrogel is undeformed and in mechanical equilibrium:

$$\mathcal{H} \rightarrow \mathcal{A}, \quad \phi_p \rightarrow \phi_{0p} \text{ as } \rho \rightarrow \infty. \quad (\text{S9h})$$

Perturbation expansion in ϵ

Working at $\mathcal{O}(1/\epsilon)$ in ϵ , (S8e) simplifies to give

$$\frac{\partial^2 \zeta^*}{\partial z^{*2}} = 0 + \mathcal{O}(\epsilon),$$

with boundary conditions

$$\xi^* \Big|_0 = \frac{\partial \xi^*}{\partial z^*} \Big|_{\mathcal{H}} = 0 \implies \xi^* = 0 + \mathcal{O}(\epsilon) \quad (\text{S10})$$

(i.e. ξ and thus u_p are not leading order terms). Similarly, to find \mathcal{P} we expand out (S8c) and then apply (S9f), yielding

$$\frac{\partial \mathcal{P}}{\partial z^*} = 0 + \mathcal{O}(\epsilon) \implies \mathcal{P} = \mathcal{P}_0 + \frac{\partial \zeta^*}{\partial z^*} \Big|_{\mathcal{H}} + \mathcal{O}(\epsilon). \quad (\text{S11})$$

Working at $\mathcal{O}(\epsilon^0)$ in ϵ and utilising (S11), (S8f) simplifies to

$$\frac{\partial^2 \zeta^*}{\partial z^{*2}} = 0 + \mathcal{O}(\epsilon). \quad (\text{S12})$$

Utilising both (S8h) and (S10), the solid phase kinematic boundary condition given in (S9) simplifies to

$$\frac{\partial \mathcal{H}}{\partial \tau} \left(1 - \frac{\partial \zeta^*}{\partial z^*} \Big|_{\mathcal{H}} \right) = \frac{\partial \zeta^*}{\partial \tau} \Big|_{\mathcal{H}}. \quad (\text{S13})$$

Thus, applying this simplified boundary condition together with (S9a), we integrate (S12) twice to obtain

$$\zeta^* = z^* \left(1 - \frac{\mathcal{A}}{\mathcal{H}} \right) + \mathcal{O}(\epsilon), \quad (\text{S14})$$

$$w_p^* = \frac{z^*}{\mathcal{H}} \frac{\partial \mathcal{H}}{\partial \tau} + \mathcal{O}(\epsilon), \quad (\text{S15})$$

$$\mathcal{P} = \mathcal{P}_0 + 1 - \frac{\mathcal{A}}{\mathcal{H}} + \mathcal{O}(\epsilon). \quad (\text{S16})$$

As a sanity check, note that from (S14), we recover $\zeta^*|_{z^*=\mathcal{H}} = \mathcal{H} - \mathcal{A}$. Utilising (S15), the polymer volume fraction mass conservation equation given in (S8a) simplifies to give

$$\frac{\partial}{\partial \tau} (\mathcal{H} \phi_p) + z^* \frac{\partial \mathcal{H}}{\partial \tau} \frac{\partial \phi_p}{\partial z^*} = 0 + \mathcal{O}(\epsilon). \quad (\text{S17})$$

This admits the separable general solution

$$\phi_p = \phi_{0p} \int \tilde{\mathcal{A}} \left(\frac{\mathcal{A}}{\mathcal{H}} \right)^{1+\sigma} z^{*\sigma} d\sigma + \mathcal{O}(\epsilon), \quad (\text{S18})$$

where $\tilde{\mathcal{A}} = \tilde{\mathcal{A}}(\rho, \sigma)$ is independent of τ and z^* . For mathematical simplicity, we will assume that ϕ_{0p} is independent of z^* when $\tau = 0$; equivalently the dominant mode in (S18) is the $\sigma = 0$ mode giving

$$\phi_p = \frac{\mathcal{A} \phi_{0p}}{\mathcal{H}} + \mathcal{O}(\epsilon). \quad (\text{S19})$$

Finally, integrating (S8b) in the z^* direction, utilising (S8d) and the boundary conditions given in (S9), yields the continuity equation for the deflection of the sheet $\overline{\mathcal{H}} = \mathcal{H} - \mathcal{A}$

$$\begin{aligned} \frac{\partial \overline{\mathcal{H}}}{\partial \tau} &= \frac{1}{\rho} \frac{\partial}{\partial \rho} \left(\rho \int_0^{\overline{\mathcal{H}}+\mathcal{A}} k \frac{\partial \mathcal{P}}{\partial \rho} dz^* \right) \\ &= \frac{\mathcal{A}}{\rho} \frac{\partial}{\partial \rho} \left(\frac{\rho k}{\overline{\mathcal{H}} + \mathcal{A}} \frac{\partial \overline{\mathcal{H}}}{\partial \rho} \right), \end{aligned} \quad (\text{S20})$$

where we have utilised (S19) to write $k(\phi)$ as a function of $\overline{\mathcal{H}}$.

SELF-SIMILAR SOLUTIONS

Small deformation limit

In the small deformation limit when $\max(\overline{\mathcal{H}}) \ll 1$, the deformation height profile $\overline{\mathcal{H}} = \overline{\mathcal{H}}_s$ satisfies

$$\frac{\partial \overline{\mathcal{H}}_s}{\partial \tau} = \nabla^2 \overline{\mathcal{H}}_s, \quad (\text{S21a})$$

with volume conservation condition

$$\int_0^\infty \rho \overline{\mathcal{H}}_s d\rho = \mathcal{V}. \quad (\text{S21b})$$

Trying a self-similar solution of the form $f_s(\eta)/\mathcal{R}_s^2$ where $\eta = \rho/\mathcal{R}_s$ and $\mathcal{R}_s = \mathcal{R}_s(\tau)$, (S21) becomes

$$-\mathcal{R}_s \frac{\partial \mathcal{R}_s}{\partial \tau} \frac{\partial}{\partial \eta} (\eta^2 f_s) = \frac{\partial}{\partial \eta} \left(\eta \frac{\partial f_s}{\partial \eta} \right). \quad (\text{S22})$$

Utilising separation of variables and the initial condition $\mathcal{R}_s(t=0) = 1$, the τ dependent terms become

$$\frac{\partial}{\partial \tau} (\mathcal{R}_s^2) = \lambda \implies \mathcal{R}_s = (1 + \lambda \tau)^{1/2}, \quad (\text{S23})$$

where λ is a constant. Similarly, using regularity of $\overline{\mathcal{H}}_s$ at $\eta = 0$ and the initial condition $\overline{\mathcal{H}}_s(\rho = 0, \tau = 0) = 1 - \mathcal{A}$, the η dependent terms become

$$\begin{aligned} -\frac{\lambda}{2} \frac{\partial}{\partial \eta} (\eta^2 f_s) &= \frac{\partial}{\partial \eta} \left(\eta \frac{\partial f_s}{\partial \eta} \right) \\ \implies \frac{\partial f_s}{\partial \eta} &= -\frac{\lambda \eta}{2} f_s \\ \implies f_s &= (1 - \mathcal{A}) \exp \left(-\frac{\lambda \eta^2}{4} \right). \end{aligned} \quad (\text{S24})$$

Applying the volume conservation condition in (S21), $\lambda = 2(1 - \mathcal{A})/\mathcal{V}$, we recover the self similar solution given in (9a) of the main text

$$\mathcal{H}_s - \mathcal{A} = \frac{1}{R_s^2} \exp \left(-\frac{(1 - \mathcal{A})}{2\mathcal{V}} \left(\frac{\rho}{R_s} \right)^2 \right), \quad (\text{S25})$$

where

$$\mathcal{R}_s = \left(1 + \frac{2(1 - \mathcal{A})\tau}{\mathcal{V}} \right)^{1/2}. \quad (\text{S26})$$

Large deformation limit

Similarly in the large deformation limit when

$$\max(\overline{\mathcal{H}}) \gg \mathcal{A},$$

the deformation height profile $\overline{\mathcal{H}} = \overline{\mathcal{H}}_l$ satisfies

$$\frac{\partial \overline{\mathcal{H}}_l}{\partial \tau} = \mathcal{A}^{1-\beta} \frac{1}{\rho} \frac{\partial}{\partial \rho} \left(\rho \overline{\mathcal{H}}_l^{\beta-1} \frac{\partial \overline{\mathcal{H}}_l}{\partial \rho} \right), \quad (\text{S27a})$$

with volume conservation condition

$$\int_0^\infty \rho \overline{\mathcal{H}}_l d\rho = \mathcal{V}. \quad (\text{S27b})$$

Trying a self-similar solution of the form $f_l(\eta)/\mathcal{R}_l^2$ where $\eta = \rho/\mathcal{R}_l$ and $\mathcal{R}_l = \mathcal{R}_l(\tau)$, (S27) becomes

$$-\mathcal{R}_l^{2\beta-1} \frac{\partial \mathcal{R}_l}{\partial \tau} \frac{\partial}{\partial \eta} (\eta^2 f_l) = \mathcal{A}^{1-\beta} \frac{\partial}{\partial \eta} \left(\eta f_l^{\beta-1} \frac{\partial f_l}{\partial \eta} \right). \quad (\text{S28})$$

Utilising separation of variables and the initial condition $\mathcal{R}_l(t=0) = 1$, the τ -dependent terms become

$$\frac{\partial}{\partial \tau} (\mathcal{R}_l^{2\beta}) = \lambda \implies \mathcal{R}_l = (1 + \lambda \tau)^{\frac{1}{2\beta}}, \quad (\text{S29})$$

where λ is a constant. Similarly, using regularity of $\overline{\mathcal{H}}_l$ at $\eta = 0$ and the initial condition $\overline{\mathcal{H}}_l(\rho = 0, \tau = 0) = 1 - \mathcal{A}$, the η dependent terms become

$$\begin{aligned} -\frac{\lambda \mathcal{A}^{\beta-1}}{2\beta} \frac{\partial}{\partial \eta} (\eta^2 f_l) &= \frac{\partial}{\partial \eta} \left(\eta f_l^{\beta-1} \frac{\partial f_l}{\partial \eta} \right) \\ \implies \frac{\partial}{\partial \eta} (f_l^{\beta-1}) &= -\frac{\lambda \eta (\beta - 1) \mathcal{A}^{\beta-1}}{2\beta}, \end{aligned}$$

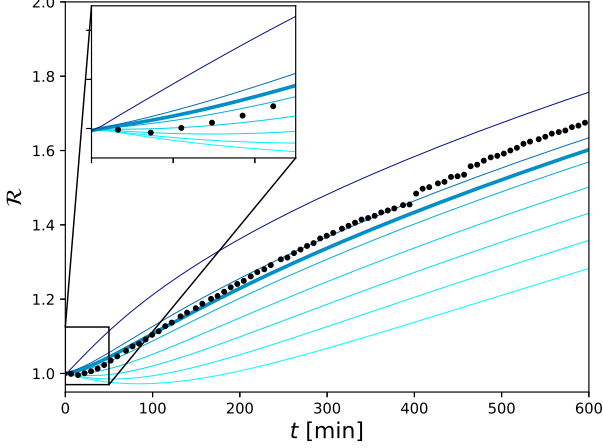


FIG. II. The experimental temporal evolution of the scaled blister radius \mathcal{R} formed by a $50 \mu\text{l}$ droplet (dots) superimposed onto a set of blue lines computed using the theoretical model, utilising the initial experimental height profile as the initial condition, where $\beta \in \{2/3, 1, 4/3, 5/3, 2, 13/6, 7/3, 3\}$. Darker blue curves correspond to larger values of β . The dimensionless time scale τ was matched to real time t using the relation $\Omega = 121.6 \text{ s mm}^{-2}$ obtained as best fit for $\beta = 13/6$ (thicker line).

hence

$$f_l = (1 - \mathcal{A}) \left(1 - \frac{\lambda(\beta - 1)\mathcal{A}^{\beta-1}}{4\beta(1 - \mathcal{A})^{\beta-1}} \eta^2 \right)^{1/(\beta-1)}. \quad (\text{S30})$$

Applying the volume conservation condition in (S21), we find

$$\lambda = \frac{2(1 - \mathcal{A})^\beta}{\mathcal{V}\mathcal{A}^{\beta-1}} \quad (\text{S31})$$

Hence, we recover the selfsimilar solution given in (9b) of the main text

$$\mathcal{H}_l - \mathcal{A} = \frac{(1 - \mathcal{A})}{R_l^2} \left(1 - \frac{(1 - \mathcal{A})(\beta - 1)}{2\beta\mathcal{V}} \left(\frac{\rho}{R_l} \right)^2 \right)^{1/(\beta-1)}, \quad (\text{S32})$$

where

$$R_l = \left(1 + \frac{2\tau(1 - \mathcal{A})^\beta \mathcal{A}^{1-\beta}}{\mathcal{V}} \right)^{1/2\beta}. \quad (\text{S33})$$

MATCHING EXPERIMENT AND MODEL

Numerical Solutions

For general \mathcal{A} , (S20) does not admit an analytic solution. Instead, we solve it numerically using the finite-

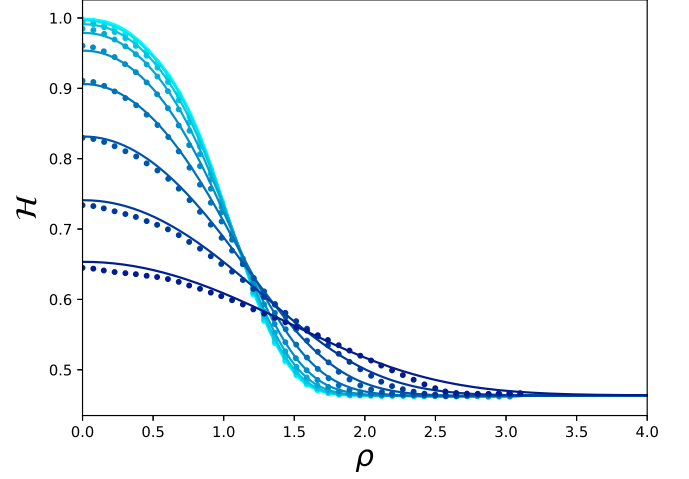


FIG. III. Comparison between experimentally observed swelling and numerical solutions of the poroelastic model, plotting the spatial dependence of the scaled height \mathcal{H} for a blister formed by a $50 \mu\text{l}$ droplet at a range of different times during the experiment. Here, experimental data is denoted by circles while numerical solutions are denoted by lines. The lightest blue curve corresponds to $t = 2 \text{ min}$ with each subsequent darker blue curve twice the previous time. Numerical solutions are generated using initial conditions taken directly from the experimental data that they are fitted against.

element software package FEniCS ([S11, S12]) on a domain $\mathcal{Q} : 0 < \rho < 100$, bounded by no flux boundary conditions. The time derivative is discretised using the backward Euler scheme

$$\frac{\partial \mathcal{H}}{\partial \tau} \approx \frac{(\mathcal{H} - \mathcal{H}_{\text{old}})}{\delta \tau}, \quad (\text{S34})$$

where \mathcal{H}_{old} is the value of \mathcal{H} at the previous time step. This leads to the weak form of (S20)

$$\int \rho \tilde{\mathcal{H}} Q d\rho = \mathcal{A}^{1-\beta} \delta \tau \int \rho (\epsilon_n + \mathcal{H})^{\beta-1} \frac{\partial \mathcal{H}}{\partial \rho} \frac{\partial Q}{\partial \rho} d\rho + \int \rho \mathcal{H} Q d\rho, \quad (\text{S35})$$

where Q is a test function and $\epsilon_n = 10^{-5}$ is introduced to avoid NaN errors in the Newton solver. The solutions were calculated with timestep $\delta \tau = 10^{-3}$ and constant grid spacing $\delta \rho = 10^{-2}$. For a given blister height profile $\mathcal{H} = \mathcal{H}(\rho, \tau)$, the effective radius $\mathcal{R} = \mathcal{R}(\mathcal{A}, \tau)$ is defined as the point where the deflection of the sheet is half the maximum deflection of the sheet, namely mathematically

$$\mathcal{R} = \left\{ \rho : \mathcal{H}(\rho) - \mathcal{A} = \frac{1}{2} \left(\max_{\bar{\rho}} (\mathcal{H}(\bar{\rho})) - \mathcal{A} \right) \right\}. \quad (\text{S36})$$

Our numerical scheme is implicitly validated by the excellent agreement between the similarity solutions and the numerics for small deformation shown in figure 3 in the main text.

Fitting procedure

We used the numerical solver described above to solve (S20) numerically, utilising an experimentally observed initial condition. To ensure compatibility with the modelling assumptions we chose an experimental profile obtained at $t = t_0$ just after the buckling instability was no-longer visible. Table i gives the associated experimental times t_0 , the corresponding frame number to enable cross referencing to the ESI and the derived values for each data set for $\{R_0, H_0, \mathcal{A}\}$.

Since numerical solutions predict the evolution of the blister as a function of dimensionless time τ with a single fitted parameter β , the poroelastic time scale $\tau_0 = \mu_f R_0^2 / \kappa_0 (K + 4G/3)$ for the propagation of the swollen layer through the hydrogel during the initial absorption of the droplet has to be determined for each experiment through fitting. Note that τ_0 can be split into a part that is experiment-dependent and a part that is experiment-independent, namely $\tau_0 = \Omega R_0^2$, where the experiment-dependent part R_0^2 is found through image analysis while the experiment-independent part $\Omega = \mu_f / \kappa_0 (K + 4G/3)$ is an unknown constant fitted to all the experimental data. Furthermore, note that we do not need to fit the elastic moduli K and G individually, decreasing the number of free variables we need to fit from the experimental data and hence increasing the strength of the fit.

In particular, for a given value for β we fitted Ω through a simultaneous fit to all the experimental data sets, minimising the least-square objective function

$$\sum_i \left\{ \text{avg}_j \left(\left(\left[\mathcal{R}_e(t_j) - \mathcal{R}_\beta \left(\frac{t_j}{\Omega R_0^2} \right) \right] / \mathcal{R}_e(t_j) \right)^2 \right) \right\}_i \quad (\text{S37})$$

Here, Ω is the fitted variable, i iterates over all datasets and j iterates over all points within a particular experimental dataset $\mathcal{R}_e(t_j)$. Both this minimisation and the subsequent linear interpolation to calculate $\mathcal{R}_\beta(t_j)$ at the experimental time steps were performed using standard NumPy and Scipy methods in Python [S13, S14].

Figure II explores graphically how varying β affects the numerical solutions of the theoretical model for how \mathcal{R} evolves temporally. As a first sweep we calculated the evolution of each profile for $2/3 \leq \beta < 3$ in increments of $1/3$. We then increased the resolution between $\beta = [2/3, 4/3]$ until we investigated $\beta = [25/12, 26/12, 27/12]$. The final values adopted were those obtained for the β with the lowest value of the objective function in (S37), namely $\beta = 2.16(0.083)$ and $\Omega = 7.3 \times 10^9 \text{ s m}^{-2}$ which corresponds to poroelastic time scales $\tau_0 = \Omega R_0^2 = 4.5 - 40.9 \text{ h}$ as shown in table i.

TABLE i. Experimental t_0 from which the initial condition for the numerical solution was obtained and corresponding values $\{H_0, R_0, \mathcal{A}\}$. The second column refers to the frame number in the corresponding raw dataset provided as ESI.

V [μl]	Frame	t_0 [min]	H_0 [mm]	R_0 [mm]	\mathcal{A}	τ_0 [h]
100	60	22.0	2.84	4.49	0.4	40.85
50	220	39.5	2.44	3.27	0.46	21.67
30	782	21.0	2.28	2.78	0.49	15.66
25	235	26.0	2.18	2.61	0.51	13.81
10	109	20.0	1.82	1.94	0.62	7.63
5	358	9.5	1.66	1.49	0.68	4.50

Profile comparison

Figure III compares the spatial dependence of the experimental profiles (dots) to the numerical predictions (lines) for the 50 μl data set. The lightest blue curve corresponds to a time of 2 min after the first frame. Each subsequent darker blue line corresponds to twice the previous time. There is generally very good agreement between experiment and theoretical predictions. However, as time increases the numerical solution over-predicts the position of the leading edge of the swollen region. We attribute this to the aforementioned alignment errors between camera and hydrogel sheet.

-
- [S1] S. B. Dalziel, *DigiFlow User Guide*, Dalziel Research Partners, <http://www.dalzielresearch.com/digiflow> (2017).
- [S2] S. Van der Walt, J. L. Schönberger, J. Nunez-Iglesias, F. Boulogne, J. D. Warner, N. Yager, E. Gouillart, and T. Yu, scikit-image: image processing in python, *PeerJ* **2**, e453 (2014).
- [S3] M. A. Etzold, P. Linden, and M. G. Worster, Transpiration through hydrogels, *Journal of Fluid Mechanics* **925** (2021).
- [S4] M. Hilder and M. van den Tempe, Diffusivity of water in groundnut oil and paraffin oil, *Journal of Applied Chemistry and Biotechnology* **21**, 176 (1971).
- [S5] D. R. Hewitt, J. A. Neufeld, and N. J. Balmforth, Shallow, gravity-driven flow in a poro-elastic layer, *J. Fluid Mech.* **778**, 335 (2015).
- [S6] A. Seminara, T. E. Angelini, J. N. Wilking, H. Vlamakis, S. Ebrahim, R. Kolter, D. A. Weitz, and M. P. Brenner, Osmotic spreading of bacillus subtilis biofilms driven by an extracellular matrix, *PNAS* **109**, 1116 (2012).
- [S7] G. T. Fortune, N. M. Oliveira, and R. E. Goldstein, Biofilm growth under elastic confinement, arXiv:2112.02540 [cond-mat.soft] (2022).
- [S8] C. W. MacMinn, E. R. Dufresne, and J. S. Wettlaufer, Large deformations of a soft porous material, *Phys. Rev. Applied* **5**, 044020 (2016).
- [S9] M. Tokita and T. Tanaka, Friction coefficient of polymer networks of gels, *The Journal of chemical physics* **95**,

- 4613 (1991).
- [S10] C. A. Grattoni, H. H. Al-Sharji, C. Yang, A. H. Mugeridge, and R. W. Zimmerman, Rheology and permeability of crosslinked polyacrylamide gel, *Journal of colloid and interface science* **240**, 601 (2001).
- [S11] M. S. Alnæs, J. Blechta, J. Hake, A. Johansson, B. Kehlet, A. Logg, C. Richardson, J. Ring, M. E. Rognes, and G. N. Wells, The fenics project version 1.5, *Archive of Numerical Software* **3**, 10.11588/ans.2015.100.20553 (2015).
- [S12] A. Logg, K.-A. Mardal, G. N. Wells, *et al.*, *Automated Solution of Differential Equations by the Finite Element Method* (Springer, 2012).
- [S13] P. Virtanen, R. Gommers, T. E. Oliphant, M. Haberland, T. Reddy, D. Cournapeau, E. Burovski, P. Peterson, W. Weckesser, J. Bright, S. J. van der Walt, M. Brett, J. Wilson, K. J. Millman, N. Mayorov, A. R. J. Nelson, E. Jones, R. Kern, E. Larson, C. J. Carey, Í. Polat, Y. Feng, E. W. Moore, J. VanderPlas, D. Laxalde, J. Perktold, R. Cimrman, I. Henriksen, E. A. Quintero, C. R. Harris, A. M. Archibald, A. H. Ribeiro, F. Pedregosa, P. van Mulbregt, and SciPy 1.0 Contributors, SciPy 1.0: Fundamental Algorithms for Scientific Computing in Python, *Nature Methods* **17**, 261 (2020).
- [S14] C. R. Harris, K. J. Millman, S. J. van der Walt, R. Gommers, P. Virtanen, D. Cournapeau, E. Wieser, J. Taylor, S. Berg, J. Smith, R. Kern, M. Picus, S. Hoyer, M. H. van Kerkwijk, M. Brett, A. Haldane, J. F. del Río, M. Wiebe, P. Peterson, P. Gérard-Marchant, K. Sheppard, T. Reddy, W. Weckesser, H. Abbasi, C. Gohlke, and T. E. Oliphant, Array programming with NumPy, *Nature* **585**, 357 (2020).